*Acta metall.* Vol. 36, No. 12, pp. 3163–3176, 1988
Printed in Great Britain. 

0001-6160/88 $3.00 + 0.00


# A QUANTITATIVE MODEL FOR THE INTERGRANULAR PRECIPITATION OF $M_7X_3$ AND $M_{23}X_6$ IN Ni–16Cr–9Fe–C–B

**R. M. KRUGER,[1] G. S. WAS,[2] J. F. MANSFIELD[3] and J. R. MARTIN[4]**

[1]3051 Phoenix Memorial Laboratory, Department of Nuclear Engineering, [2]213 Cooley Building, Department of Nuclear Engineering, [3]Electron Microbeam Analysis Laboratory, University of Michigan, Ann Arbor, MI 48109 and [4]Surface Analysis Central Facility, Center for Materials Science and Engineering, Massachusetts Institute of Technology, Cambridge, MA 02139, U.S.A.

(*Received* 8 *August* 1987; *in revised form* 16 *March* 1988)

**Abstract**—A thermodynamic model has been constructed to explain the details of grain boundary chemistry in Ni–16 Cr–9 Fe doped with carbon and boron. In this model, Gibbs free energy of the precipitates is calculated using an ideal solution model for both the metallic and non-metallic sub-lattices in $M_{23}X_6$ and $M_7X_3$, and the activities of the five species in the matrix are calculated using a Kohler equation formalism involving only binary terms. The parameters required by the model are based solely on data on the constituent binary and ternary subsystems. The model yields correct results for the compositions of intergranular, Ni + B-rich $M_{23}X_6$ (M > 80 at.% Ni, X ≈ 100 at.% B) as well as Cr + C-rich $M_7C$-rich $M_7C_3$ at 873 K and 973 K. The result that $M_{23}X_6$ is rich in Ni and B only occurs when the chemical activities in the matrix are those for a grain boundary in equilibrium with $Cr_7C_3$, which implies that Ni + B-rich $M_{23}X_6$ develops as a consequence of intergranular $Cr_7C_3$ and the resultant depletion of Cr at the grain boundary. The model does not successfully explain the precipitation of B rich $M_{23}X_6$ and $M_7X_3$ at 1173 or 1273 K.

**Résumé**—Nous avons élaboré un modèle thermodynamique pour expliquer les détails de la chimie des joints de grains dans Ni–16 Cr–9 Fe dopé au carbone et au bore. Dans ce modèle, on calcule l'énergie libre de Gibbs des précipités à l'aide d'un modèle de solution idéale pour les sous-réseaux métalliques et non métalliques de $M_{23}X_6$ et de $M_7X_3$, et l'on calcule l'activité des cinq constituants de la matrice à l'aide d'un formalisme d'équations de Kohler ne comportant que des termes binaires. Les paramètres nécessaires sont uniquement basés sur les caractéristiques des sous-systèmes binaires et ternaires de base. Ce modèle fournit des résultats corrects pour la composition—à 873 K et à 973 K—des deux composés intergranulaires: $M_{23}X_6$ riche en nickel et en bore (M > 80% en atomes de nickel, X ≈ 100% en atomes de bore) et $M_7C_3$ riche en chrome et en carbone. L'enrichissement de $M_{23}X_6$ en nickel et en bore n'a lieu que lorsque les activités chimiques dans la matrice sont les mêmes que dans un joint de grains en équilibre avec $Cr_7C_3$, ce qui implique que $M_{23}X_6$ riche en nickel et en bore se développe à cause de $Cr_7C_3$ intergranulaire et de manque en chrome qui en résulte dans le joint de grains. Ce modèle n'explique pas de façon satisfaisante la précipitation de $M_{23}X_6$ riche en bore et de $M_7X_3$, à 1173 ou 1273 K.

**Zusammenfassung**—Es wird ein thermodynamisches Modell zur Beschreibung der Einzelheiten der Korngrenzchemie in Kohlenstoff- und Bor-dotiertem Ni–16 Cr–9 Fe entwickelt. In diesem Modell wird die freie Enthalpie der Ausscheidungen berechnet, indem ein ideales Lösungsmodell sowohl für die metallischen wie auch die nichtmetallischen Untergitter in $M_{23}X_6$ und $M_7X_3$ benutzt wird; außerdem werden die Aktivitäten der fünf Atomsorten in der Matrix mit einem Kohler-Gleichungsformalismus, der nur binäre Terme enthält, berechnet. Die vom Modell geforderten Parameter beruhen auf Daten ausschließlich der binären und ternären Subsysteme. Das Modell ergibt richtige Ergebnisse für die Zusammensetzung des intergranularen Ni + B-reichen $M_{23}X_6$ (M > 80 At.-% Ni, X ≈ 100 At.-% B) und des Cr + C-reichen $M_7X_3$ bei 873 und 973 K. Das Ergebnis, daß $M_{23}X_6$ reich an Ni und B ist, tritt nur auf, wenn die chemischen Aktivitäten in der Matrix diejenigen der Korngrenze im Gleichgewicht mit $Cr_7C_3$ sind; das heißt, daß Ni + B-reiches $M_{23}X_6$ sich als eine Folge des intergranularen $Cr_7C_3$ bildet mit der entsprechenden Verarmung an Cr an der Korngrenze. Das Modell kann die Ausscheidung von B-reichem $M_{23}X_6$ und $M_7X_3$ bei 1173 oder 1273 K nicht erfolgreich erklären.

## 1. INTRODUCTION

When Ni base alloys such as Inconel 600 are heat treated at temperatures below the carbon solvus, chromium-rich carbides precipitate at the grain boundaries. This causes a reduction in the Cr concentration at the boundaries [1]. This chromium depletion is significant, because it renders the alloys susceptible to intergranular corrosion and intergranular stress corrosion cracking in some environments [2–6]. Initially, the Cr concentration at the grain boundary ($x_{Cr,gb}$) is thermodynamically controlled by the paraequilibrium between the precipitate and the matrix [1]. Theoretically, $x_{Cr,gb}$ can be altered by a change in precipitate type. For example, replacing $Cr_7C_3$ by $Cr_{23}C_6$ would raise the grain

boundary Cr concentration by approximately 5 at.% [1, 7].

Both types of intergranular carbides have been found in Ni base alloys of the approximate composition Ni–16 Cr–9Fe. Studies of Inconel 600 (Ni–15.8 Cr–7.2 Fe–0.2 Mn–0.2 Si–0.04 C), Nimonic 75 (Ni–20 Cr–5 Fe–0.4 Ti–0.083 C), and high purity Ni–16 Cr–8 Fe–0.0015 C indicate that their grain boundaries are mainly covered by $Cr_7C_3$ [7, 8, 9, 10]. Small amounts of intergranular $M_{23}X_6$ (M = transition metal, X = non-metal) have also been identified in these alloys. Belo *et al.* found $M_{23}C_6$ in Ni–16 Cr–8 Fe–0.0015 C that received a heat treatment of 973 K for 1 h, and not in material that received a heat treatment of 973 K for 17 h or longer. Airey found $M_{23}X_6$ in Inconel 600 [11]. The only studies of Inconel 600 in which $M_{23}X_6$ is reported to be a major intergranular precipitate are those of Nagano *et al.* and of Hall and Briant [7, 12]. The materials with high amounts of $M_{23}X_6$ were unusual in that they contained over 20 wppm B, which is a high concentration as compared to other studies of Inconel 600. Hall and Briant determined that at least some of the $M_{23}X_6$ is rich in Ni and B. Alloys with similar compositions to Inconel 600 and containing predominantly intergranular $M_{23}X_6$, instead of $Cr_7C_3$, include Inconel X-750 (Ni–15.5 Cr–7 Fe–2.5 Ti–0.95(Cb + Ta)–0.7 Al–0.04 C), and Nimonic 80 (Ni–19.5 Cr–5 Fe(max)–2.25 Ti–2 Co(max)–1.13 Al–0.1 C(max)) [13, 14].

The purpose of this work is to understand the factors controlling the precipitation of Cr + C-rich $M_7X_3$ and Ni + B-rich $M_{23}X_6$ in Ni–16 Cr–9 Fe–0.03 C–0.005 B, as well as the absence of intergranular Cr + C-rich $M_{23}X_6$. This will be accomplished by experiment determination of the composition of the intergranular precipitates found in Ni–16 Cr–9 Fe–0.03 C with and without B and construction of a thermodynamic model for precipitate composition. If the model results are consistent with experimental observations, and if it can be shown that kinetic limitations are unimportant, then the precipitate composition is thermodynamically controlled.

## 2. EXPERIMENTAL

### 2.1. Materials

High purity heats of Ni–16 Cr–9 Fe were prepared by the Materials Preparation Center, Ames Laboratory, Iowa State University. These were doped, as specified, with C and B. The chemical analyses of all heats referred to in this work are listed in wt% in Table 1. Cast ingots (13 mm diameter) were swaged down to 3.05 mm rod. Heat treatments were performed in a Lindberg Model 54232 tube furnace in an argon atmosphere. A high temperature solutionizing anneal was provided first. Typically, this was 1373 K for 20 min, but 1473 K for 20 min was also used. The low temperature heat treatments referred to in this work include 873 K for 250 h, 973 K for 1 h, 973 K for 10 h, and 1073 K for 25 min. Samples were water quenched at the conclusion of each annealing or heat treatment step.

Table 1. Compositions of alloys used to study intergranular precipitation in Ni–16 Cr–9 Fe (wt%)

| Alloy Designation | Ni | Cr | Fe | C | B |
|---|---|---|---|---|---|
| Undoped | 74.2 | 16.8 | 9.0 | 0.0008 | 0.00003 |
| C-doped | 74.8 | 16.1 | 9.1 | 0.026 | — |
| B-doped | 74.5 | 16.4 | 9.1 | 0.029 | 0.005 |

### 2.2. Scanning transmission electron microscopy

*2.2.1. Specimen preparation.* Thin foils were used for precipitate structure identification, electron energy loss spectroscopy (EELS) measurements of precipitate composition, and Cr depletion measurements. Following heat treatment, the 3 mm rod was cut into thin wafers (approximately 0.40 mm thick) with a slow speed diamond saw. The wafers were thinned on both sides using 320–600 grit SiC paper to a final thickness of 0.12 mm, with a range of 0.6–0.14 mm. The thin discs were made into foils using a single jet thinner (South Bay Technology Model 550B) and an electrolyte of 70% methanol, 20% perchloric acid (70% $HClO_4$), and 10% butylcellosolve at 233 K.

Extraction replicas were used to measure the metal contents of precipitates and to obtain additional information on grain boundary structure. Metallographic mounts were polished on a grinding wheel through 600 grit paper, then polished with levigated alumina (13–20 $\mu$m), and finally with colloidal silica (Syton HT-50). The polished mounts were etched in a solution of 98% methanol + 2% hydrochloric acid (37% HCl) for 15 s at 6 V. The etched samples were carbon coated until a brown film was visible and then scratched deeply so that the film was divided into 2.3 $mm^2$ squares. These were re-etched until the individual carbon squares separated. These carbon squares were floated onto 3 mm diameter, 200 mesh aluminum grids and rinsed in methanol. If the film was rolled up, it was rinsed a second time in distilled water, which allowed it to unroll and break up into smaller pieces.

*2.2.2. Microscopy.* The metallic composition of precipitates was measured primarily by $X$-ray energy dispersive spectroscopy (EDS) of extraction replicas. The work was performed on a JEOL 100-CX scanning transmission electron microscope (STEM) at the University of Michigan using a Gatan double tilt cold stage equipped with an aluminum sample cup and tip. This was done to minimize sample fluorescence by hard $x$-rays (i.e. $CuK_{\alpha,\beta}$) produced in the stage. Measurements were taken in a transmitted electron imaging mode with a $LaB_6$ electron emitter and a focused 10 nm diameter electron beam. Spectra were acquired in 30–200 s on at least 12 individual precipitates. Visible contamination of the precipitates was rare, so the stage was operated at room temperature.

The non-metallic composition of precipitates was measured by electron energy loss spectroscopy with a Gatan Model 607 EELS Spectrometer on a Philips 420 STEM. The measurements were performed on precipitates that were adjacent to foil perforations. The foils that were prepared for this purpose were intentionally etched at the grain boundaries (by using a low polishing current) in order to maximize the number of exposed precipitates. Spectra were acquired using 1 eV per channel, 400–1000 channels, and dwell times of 100–300 ms per channel. For each case of interest, spectra were obtained on at least 5 individual precipitates. All spectra were processed using a zero-integral top-hat filter designed to enable the identification of small peaks while suppressing the background [15]. The composition of the matrix at the grain boundary was obtained via EDS measurements of thin foils at the JEOL 100CX STEM. Measurements were made using the Gatan double tilt cold stage described earlier. It was operated at 153 K to prevent the build-up of contamination at the locations being analyzed.

Spectra were acquired at precipitate free boundary segments mid-way between precipitates, and also at a succession of points away from the grain boundary. Six or more grain boundary segments were examined for each case of interest. Spectrum collection times ranged between 30 and 200 s, the time being set to ensure at least 2000 counts in the $CrK_\alpha$ and $FeK_\alpha$ X-ray peaks. X-ray peak counts were converted to elemental concentrations using the Cliff–Lorimer technique [16].

### *2.3. Auger electron spectroscopy*

Auger electron spectroscopy (AES) was used to confirm the presence of B in grain boundary precipitates. Tensile samples were machined from the 3.05 mm diameter (0.12″) rod stock following heat treatment. The gauge section was made using a surface grinder, and was approximately 0.010″ thick and 0.060″ wide [17]. The overall sample length was 0.575″, with grips of 0.075″ and 0.15″ in length on either end. Grain boundary embrittlement due to $H_2$ was obtained by cathodically charging the specimens at a current density of 10–20 mA/cm$^2$ in a solution of 1 N $H_2SO_4$ + 2.0 mg per liter $AsO_3$ (or $NaAsO_2$) held at 333 to 343 K. Charging times ranged from 16 to 36 h.

Auger electron spectroscopy was performed using a Physical Electronics model PHI 590 Scanning Auger Microprobe. The charged samples were strained *in situ* at $10^{-4}$ cm/s in a slow extension rate stage until they fractured. At the time of fracture, the vacuum was always better than $6.0 \times 10^{-9}$ torr, and was usually between $2.0–3.0 \times 10^{-9}$ torr. Analysis was performed using a 3 kV electron beam and a beam current of 200–255 nA. This beam voltage was chosen in order to maximize the relative sensitivity for the detection of B. The beam was rastered on the center of grain faces over a 400 $\mu$m$^2$ area. The raster mode was chosen over point mode in order to minimize scatter in the data.

Data were collected in a multiplex analysis mode. Energy windows were set up for C, O, Cr, Fe, Ni, and either B or N. In a few cases, a separate window was set up for Ti instead of Fe.

Sputtering was performed to determine whether the B present on grain boundaries was (a) contained in precipitates, (b) segregated at the matrix-matrix or precipitate-matrix interfaces, or (c) both. Sputtering using 2 kV $Ar^+$ ions was performed immediately after analysis of the fresh fracture surfaces was completed. The flux of the sputtered ions was not known, but was estimated as 50 $\mu$A/cm$^2$. The area of the sputtering beam was approximately 2 mm$^2$, and sputtering times of 10–15 s were used. Each sputtering interval was followed by a standard 12 mm multiplex analysis. Although the Ar ion beam direction was almost tangential to the fracture surface, sputtering did occur rapidly.

## 3. EXPERIMENTAL RESULTS

### *3.1. Precipitate identification*

Following low temperature heat treatments, the grain boundaries of both the C-doped and B + C-doped alloys contained precipitates with the $Cr_7C_3$ structure. This chromium carbide is described as pseudo-hexagonal, with $a_0 = 1.3982$ nm and $c_0 = 0.506$ nm, and with 80 atoms per until cell [18]. No other types of intergranular precipitates were found in the C alloy. Figure 1 shows a selected area diffraction pattern (SADP) obtained from a $Cr_7C_3$ precipitate. The pattern contains streaks due to the stacking faults that are typically found in $Cr_7C_3$ [18].

In the heat treated B + C-doped alloy, intergranular $Cr_7C_3$ was accompanied by $M_{23}X_6$. The crystal structure of $M_{23}X_6$ is face centered cubic, with 116 atoms per unit cell and a lattice parameter of approximately 1.06 nm [19, 20]. The precipitate was identified only on grain boundaries in the

Fig. 1. Selected area diffraction pattern for $Cr_7C_3$ in C-doped alloy that was annealed (1373 K, 20 min) and heat treated (973 K, 100 h).

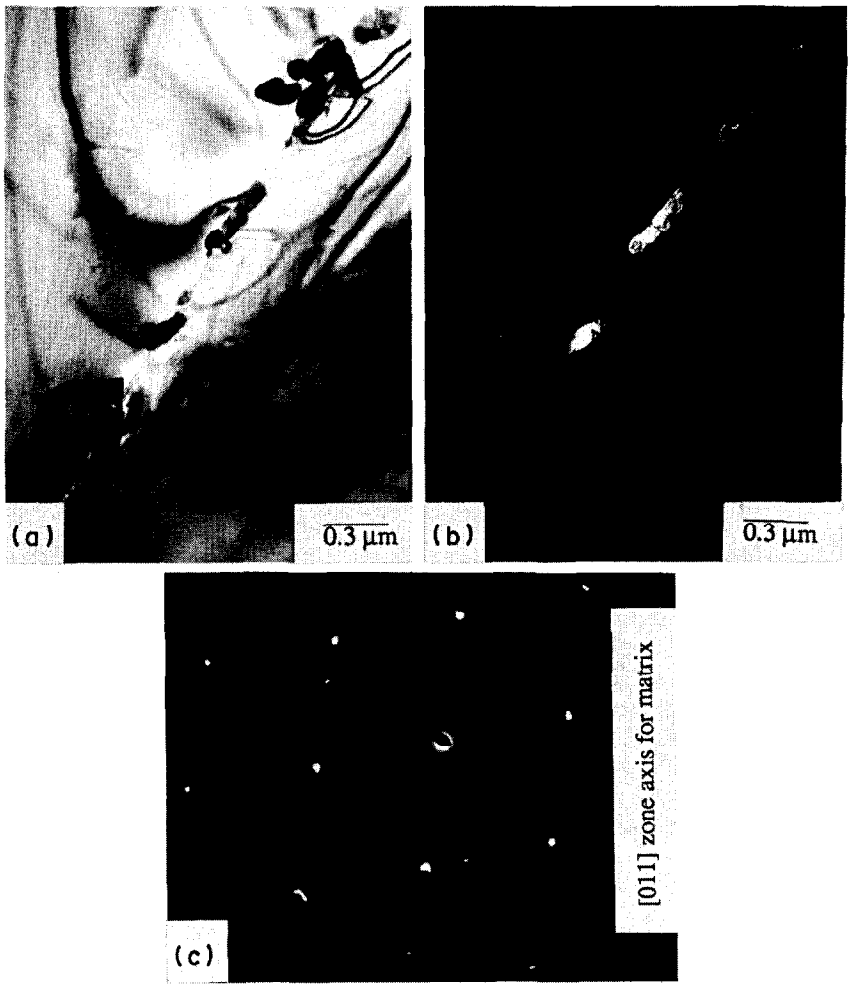


Fig. 2. Intergranular precipitation in B + C doped alloy that was annealed (1273 K, 60 min) and heat treated (973 K, 10 h): (a) bright field image, (b) dark field image, and (c) SADP of central precipitates on this grain boundary. Central precipitates are $M_{23}X_6$, and precipitates away from center are $Cr_7C_3$.

B + C-doped alloy, and never on the grain boundaries in the C-doped alloy. Figure 2 contains the bright field and dark field images of a grain boundary that contains $M_{23}X_6$, as well as the diffraction pattern used for this identification. Aside from having the correct indices, this SADP shows the same cube-on-cube orientation relationship between the matrix and $M_{23}X_6$ as in 304SS [21, 22]. This orientation relationship was invariably found on one side of the grain boundary or the other. The identification of the $M_{23}X_6$ crystal structure is further substantiated by convergent beam diffraction patterns. Figure 3 contains a CBDP taken of a grain boundary precipitate in the B + C-doped alloy. This pattern is similar to that of $Cr_{23}C_6$ on the [011] zone axis. However, the precipitate is not $Cr_{23}C_6$. As reported below, it is more nearly $Ni_{23}B_6$.

Individual grain boundaries in the B + C-doped alloy contain both types of precipitate. This can be seen in Fig. 2, in which the dark field image only reveals the central precipitates appearing on the bright field image, and not the others. From this (and confirmation via the SADPs of the neighboring precipitates) it can be seen that $M_{23}X_6$ and $Cr_7C_3$ can coexist on the same grain boundary. These two kinds of precipitates can appear adjacent to each other, as


Fig. 3. Convergent beam diffraction pattern for intergranular $M_{23}X_6$ precipitate. B + C-doped alloy was annealed (1473 K, 20 min) and heat treated (973 K, 10 h).


Fig. 4. Grain boundary containing both $M_{23}X_6$ and $Cr_7C_3$ in B + C-doped alloy that was annealed (1373 K, 20 min) and heat treated 873 K, 250 h.

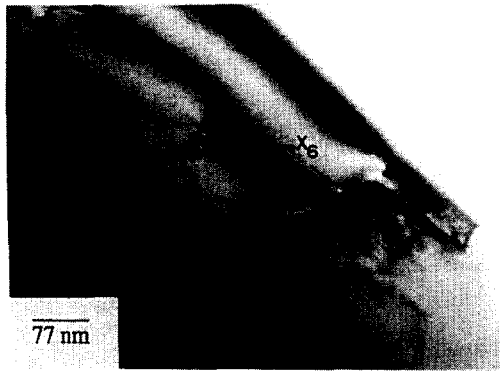


Fig. 6. $M_{23}X_6$ precipitates on grain boundary in B + C-doped alloy. Alloy received anneal of 1373 K for 20 min.

illustrated by the micrograph in Fig. 4. Here the $M_{23}X_6$ displays moire fringes, and is found in between $Cr_7C_3$ precipitates. The moire patterns due to $M_{23}X_6$ overlaying the matrix are analogous to patterns seen for $Cr_{23}C_6$ on 304SS [21, 22]. Since the lattice parameters of $M_{23}X_6$ and $Cr_{23}C_6$ are similar (approximately 1.06 nm), as are those of Ni–16 Cr–9 Fe and stainless steel (0.356 vs 0.359 nm), one would expect similar moire effects. Figure 4 demonstrates that $M_{23}X_6$ and $Cr_7C_3$ can sometimes be distinguished by image contrast, although not by their shapes.

Solution annealing at 1373 or 1473 K yields precipitate free grain boundaries in the C-doped alloy. However, intergranular precipitates are found in the B + C-doped alloy following annealing. Precipitates with the $Cr_7C_3$ structure are the predominant kind (Fig. 5). In addition to these, $M_{23}X_6$ forms, as shown in Fig. 6, and has been identified at both 1373 and 1473 K.

The metallic components of the intergranular precipitates were measured by EDS, as summarized in Table 2. The most significant results are as follows. First, the $M_7X_3$ precipitates were very rich in Cr and poor in Fe and Ni in both the C-doped and B + C-doped alloys. The Fe and Ni contents of these precipitates increased with increasing temperature. This trend could be followed up to the annealing temperatures for alloy B + C, which yielded precipitates at least up to 1473 K. The second important result is that *all* $M_{23}X_6$ grain boundary precipitates, which were only found in alloy B + C, are rich in Ni, and poor in Cr and Fe. No Cr-rich $M_{23}X_6$ was ever seen on grain boundaries.

EELS spectra were taken on $M_{23}X_6$ in order to determine its light element content. As shown in Fig. 7(a), a small peak due to B is present at 188 eV. This edge is small enough to be an artifact, but it appears reproducibly. No such K edge can be seen for C at 284 eV unless the precipitate is visibly contaminated. Since at least one of these two elements must be present, the best interpretation is that boron is the major interstitial element present. Application of a digital filter to the full spectrum yields peaks at electron energy losses corresponding to B, Cr, Fe, and Ni, as in Fig. 7(b), but no signal corresponding to C. From such spectra, it can be concluded that $M_{23}X_6$ is rich in B and Ni. This conclusion is consistent with the results of the EDS measurements presented above and with the precipitate composition model results. A similar B peak could not be found in the $M_7X_3$ precipitates that appeared in these heat treatments [23].

Boron also appears in high temperature precipitates. Figure 8(a) is a representative spectrum for a

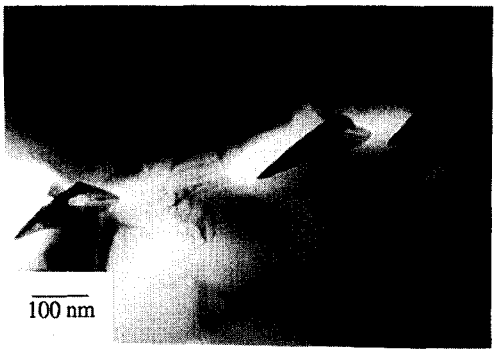


Fig. 5. $M_7X_3$ precipitates on grain boundary in B + C-doped alloy. Alloy received anneal of 1473 K for 20 min.

Table 2. EDS results for the metallic contents of intergranular precipitates in C-doped and B + C-doped Ni–16 Cr–9 Fe alloys (results expressed in %)

| Heat treatment | Element | Alloy C | Alloy B + C | |
|---|---|---|---|---|
| | | $M_7X_3$ | $M_7X_3$ | $M_{23}X_6$ |
| 1373 K, 20 min + 873 K, 250 h | Cr | 99.7 ± 0.2 | 96.1 ± 1.8 | 2.4 ± 1.9 |
| | Fe | 0.3 ± 0.1 | 2.1 ± 1.0 | 2.7 ± 2.2 |
| | Ni | 0.0 | 1.8 ± 0.8 | 94.9 ± 3.8 |
| 1373 K, 20 min + 973 K, 10 h | Cr | 95.4 ± 0.7 | 94.0 ± 1.5 | 10.7 ± 4.7 |
| | Fe | 2.3 ± 0.4 | 3.0 ± 0.6 | 7.8 ± 2.9 |
| | Ni | 2.3 ± 0.5 | 3.0 ± 1.0 | 81.5 ± 6.1 |
| 1373 K, 20 min | Cr | – | 81.7 ± 4.0 | 25.1 ± 4.4 |
| | Fe | — | 4.8 ± 1.0 | 6.2 ± 0.7 |
| | Ni | — | 13.5 ± 3.0 | 68.7 ± 3.9 |

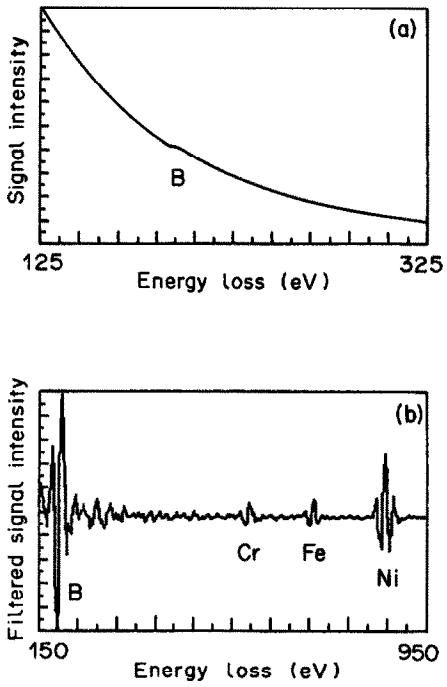


Fig. 7. EELS spectrum for intergranular $M_{23}X_6$ in annealed (1373 K, 20 min) and heat treated (973 K, 10 h) B + C-doped alloy: (a) energy window from original spectrum, and (b) digitally filtered spectrum.

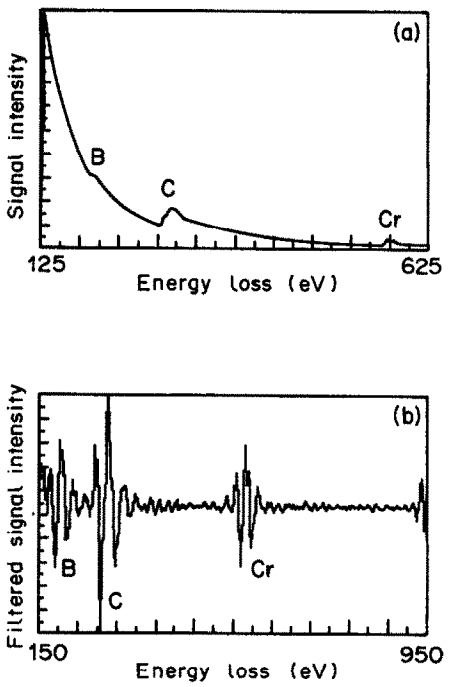


Fig. 8. EELS spectrum for $M_7X_3$ grain boundary precipitate in annealed (1373 K, 20 min) B + C-doped alloy: (a) energy window from original spectrum, and (b) digitally filtered spectrum.

$M_7X_3$ precipitate that appeared at 1373 K. The filtered spectrum is shown in Fig. 8(b). Here, the peak for B is prominent despite the appearance of a large C peak. This C peak is at least partially due to beam induced contamination. Unfortunately, no contamination free spectra were obtained on the $M_7X_3$ precipitates appearing in the annealed material. The confirmation of B in these $M_7X_3$ grain boundary precipitates is significant, proving that B plays a direct role in their formation.

### 3.2. Grain boundary composition

*3.2.1. Major elements.* Measurements of grain boundary composition were made on both the C-doped and B + C-doped alloys (Table 3). The chromium depletion minima ($x_{Cr,gb}$) were obtained by adjusting the measured values to account for the finite diameter of the beam and for beam broadening [1, 23]. Regarding the results presented here, the differences in $x_{Cr,gb}$ between the two alloys were relatively small, and are attributable to scatter. The largest difference is 1.5 at.%, which occurs for the 973 K, 10 h heat treatment. This may be significant, because the mean values are over one standard deviation apart.

The concentration ratio of Fe to Ni was obtained along with $x_{Cr,gb}$. Typically, the atom fraction ratio of iron to nickel ($x_{Fe}/x_{Ni}$) was 0.142 in the 973 K, 10 h cases and 0.158 in the 873 K, 250 h cases. These results were fairly uniform among all of the heats, and can be compared with the bulk values of 0.127. Thus, there was a slight enrichment of Fe relative to Ni at the grain boundaries.

*3.2.2. Boron.* Auger electron spectroscopy was used to confirm the presence of B in precipitates in the B + C alloy. This was done by measuring both fresh and sputtered surfaces, and comparing the results, as shown in Table 4. Because C and O were adsorbed during the analyses, data are presented as fractional surface concentrations. The fractional surface concentrations for the major alloying elements, Cr, Fe, and Ni, were calculated without accounting for any of the minor elements. In this table, results are given for specimens subject to two separate heat treatments. It can be seen that, in both cases, the B concentration was approximately halved by the first 10 s of sputtering, and that further sputtering had little or no additional effect on it. These results indicate that B is present both as a segregant and as a precipitate.

Table 3. Cr depletion minima measured via STEM for C-doped and B + C-doped alloys (results expressed in atom % Cr)

| Heat treatment | Alloy C | Alloy B + C |
|---|---|---|
| 873 K, 250 h | 6.3 ± 0.5 | 6.6 ± 0.4 |
| 973 K, 1 h | 8.9 ± 0.7 | 10.3 ± 0.4 |
| 973 K, 10 h | 9.1 ± 0.5 | 9.5 ± 0.9 |
| 1073 K, 25 min | 10.1 ± 0.3 | — |

*Following solution anneal at 1373 K for 20 min.

Table 4. Auger electron spectroscropic data for sputtered fracture surfaces of B + C doped alloy (all measured surface concentrations are normalized as shown and multiplied by 100)

| Heat treatment | Sputter time(s) | B / (B + Cr + Fe + Ni) | Cr / (Cr + Fe + Ni) | Fe / (Cr + Fe + Ni) | Ni / (Cr + Fe + Ni) |
|---|---|---|---|---|---|
| ANN + 873 K, 250 h | 0 | 6.8 | 18.2 | 7.8 | 74.0 |
| | 10 | 3.5 | 16.0 | 9.1 | 74.9 |
| | 30 | 2.5 | 16.1 | 9.1 | 74.8 |
| | 75 | 2.4 | 15.6 | 8.8 | 75.7 |
| ANN + 973 K, 10 h | 0 | 4.8 | 17.3 | 8.2 | 74.4 |
| | 10 | 2.2 | 15.2 | 8.0 | 76.8 |
| | 30 | 1.5 | 15.1 | 9.2 | 75.7 |
| | 60 | 2.5 | 14.6 | 8.7 | 76.7 |

The sputtering of the fresh fracture surfaces was performed with the $Ar^+$ beam nearly parallel to the fracture surface, as dictated by the geometry of the machine. Sputtering is not usually done at glancing angles, and it was not certain initially whether any sputtering could occur. The data on B indicate that this technique was successful.

The presence of Ni + B-rich precipitates is further substantiated by Auger results on a B-free, C-doped alloy [23, 24]. When B is absent, the fresh fracture surfaces yield substantially lower Auger signals for segregated Ni that cannot be accounted for by measured differences in Cr-depletion, so that the results for the B + C-doped alloy are consistent with the presence of abundant Ni + B-rich $M_{23}X_6$ at the grain boundaries.

## 4. MODELS

In this section, thermodynamic models will be developed to describe (1) the activities of all species in the matrix, (2) the composition of the matrix at the grain boundary, and (3) the composition of grain boundary precipitates. The primary reason for modelling is to understand the experimental results for precipitate composition. As will be shown, the model used in the calculation of precipitate compositions requires the calculation of the activities of all species present in the matrix at the grain boundary. Therefore, the methods used to calculate chemical activities both at and away from the grain boundary will be presented first.

### *4.1. Matrix activity*

The chemical activities of all species present in the matrix will be required in the models for grain boundary composition and precipitate composition. The calculation of matrix activities is based on earlier work, in which time dependent Cr concentration profiles were calculated on a combined thermodynamic-kinetic basis [1]. The thermodynamic aspect of the previous work involved calculating the activities of C, Cr, Fe, and Ni in the matrix to determine the Cr concentration at the grain boundary. The calculation of matrix activities is based on a generalized Kohler equation, which describes the free energy per mole in the matrix as a function of composition [25, 26]. The Kohler equation is written as

$$G_{\text{mix}} = \sum_i x_i G_i + RT \sum_j x_j \ln x_j + \sum_i \sum_j g_{ij} \frac{x_i^2 x_j}{x_i + x_j} \quad (1)$$

where $G_{\text{mix}}$ is the molar free energy of the matrix, $G_i$ is the free energy of species $i$ in the face centered cubic state, $x_i$ is the mole fraction of species $i$, and $g_{ij}$ is the binary interaction parameter for the pair $i$–$j$. The first two summations represent the ideal molar Gibbs free energy of the matrix, while the double summation represents the excess molar Gibbs free energy.

The calculation of the activity of any species is based on equation (1). This equation can be used to derive the chemical potential, from which the activity can be calculated via the relation

$$a_i = \exp(\mu_i / RT). \quad (2)$$

As shown in Ref. [23], the chemical potential can be derived from equation (1), and is given by

$$\mu_i = G_i + RT \ln x_i - G^{\text{ex}} + \sum_k R_k [g_{ki} x_k R_k + g_{ik} x_i (R_k + 1)] \quad (3)$$

where $\mu_i$ is the chemical potential of species $k$ and $R_k = x_k/(x_i + x_k)$.

The only parameters required in the calculation of the activities are the $G_i$ and the $g_{ij}$, and are listed in Table 5. In the cases where $g_{ij} = g_{ji}$, the available data were not highly detailed for the pair of elements $i$-$j$, and were fitted using a regular solution model (in which $g_{ij} = g_{ji}$). In the cases involving B or C, the value of $g_{\text{XM}}$ (X = non-metal, M = metal) is of minor importance, because $x_{\text{B}}$ and $x_{\text{C}}$ are small [see equation (3)].

Two basic changes have been made in the data set that was originally used in the calculation of activities [1]. The first change concerns the values of $g_{ij}$ used for carbon. The original approach taken was to use $g_{ij}$ from the literature on the binary systems Cr–C, Fe–C, and Ni–C [27, 28], and to add a ternary term to equation (1) for the calculation of $\mu_{\text{C}}$ to enable accurate simulation of the carbon solvus curve of Inconel 600. This approach worked very well, but the data used to calculate the carbon activity coefficient was chosen for a particular alloy and could not be

Table 5. Parameters for the thermodynamic model of the matrix

| $i$ | $G_i$(J/g-mol) | Reference |
|---|---|---|
| B | 43514.0–12.217 T | 28 |
| C | 138490.0–14.644 T | 27 |
| Cr | 10640.0 + 0.6276 T | 29 |
| Fe | 0 | by definition |
| Ni | 0 | by definition |

| $i$–$j$ | $g_{ij}$(J/g-mol) | Reference |
|---|---|---|
| B–C | $-83{,}680.0$ | 28 |
| B–Cr | $37{,}656.0 + 20.92\,T$ | 28 |
| B–Fe | $-188{,}280.0 + 108.78\,T$ | 28 |
| B–Ni | $-133{,}888.0 + 83.68\,T$ | 28 |
| C–B | $-83680.0$ | 28 |
| C–Cr | $-290704.0 + 114.433\,T + 9.4772\,10^{-3}\,T^2 - 2.60715\,10^{-6}\,T^3$ | 23 |
| C–Fe | $169941.0 - 2.536\,T$ | 23 |
| C–Ni | $-91587.0 + 14.033\,T$ | 23 |
| Cr–B | $-62670.0 + 6.276\,T$ | 28 |
| Cr–C | $-290704.0 + 114.433\,T + 9.4772\,10^{-3}\,T^2 - 2.60715\,10^{-6}\,T^3$ | 23 |
| Cr–Fe | $7405.0 - 6.276\,T$ | 29 |
| Cr–Ni | $-8368.0 + 4.696\,10^{-3}\,T^2 - 7.8027\,10^{-6}\,T^3$ | 29 |
| Fe–B | $-96232.0 + 62.76\,T$ | 28 |
| Fe–C | $-63678.0 - 14.096\,T + 4.8808\,10^{-2}\,T^2 - 1.0401\,10^{-5}\,T^3$ | 23 |
| Fe–Cr | $7405.0 - 6.276\,T$ | 29 |
| Fe–Ni | $2092.0 - 3.8314\,10^{-3}\,T^2 + 1.6338\,10^{-6}\,T^3$ | 29 |
| Ni–B | $-79496.0 + 41.84\,T$ | 28 |
| Ni–C | $-91587.0 + 14.033\,T$ | 23 |
| Ni–Cr | $-25104.0 + 9.4772\,10^{-3}\,T^2 - 2.60715\,10^{-6}\,T^3$ | 29 |
| Ni–Fe | $-34881.0 - 2.4404\,10^{-2}\,T + 4.8808\,10^{-2}\,T^2 - 1.0401\,10^{-5}\,T^3$ | 29 |

expected to be applicable to other alloys. The new approach is to omit the ternary term, and to use literature data on $a_C$ in the Ni–Cr–C and Ni–Fe–C systems to derive a different set of $g_{ij}$ for C. In this way, the calculation of $a_C$ is not based on a particular system but rather on data that have been compiled for the component ternary systems. The new $g_{ij}$ were derived using the activity of C in Ni–Cr–C as found by Lobl *et al.* and in Ni–Fe–C as found by Wada *et al.* [23, 30, 31]. The second change in the data base used to calculate matrix activities has been to include the $G_i$ and $g_{ij}$ for B found in the literature [28]. The complete set of interaction coefficients and the $G_i$ are shown in Table 5.

### 4.2. Grain boundary composition

The activities of all 5 components in the matrix at the grain boundary are required by the precipitate composition model. In order to obtain these activities, the composition of the matrix at the grain boundary must be calculated. The validity of the set of activities can then be tested by comparing the calculated composition with the measurements described above. The assumptions used in these calculations, with two exceptions, are essentially the same as those used in the DEPLETE model for the calculation of the Cr depletion profile [1]. The major change is that the ratio $a_{Fe}:a_{Ni}$ is now assumed constant. This replaces a prior assumption that stated that the ratio $x_{Fe}:x_{Ni}$ is constant. By using a constant activity ratio, the concentrations of Fe and Ni at the grain boundary are calculated in a way that permits the ratio $x_{Fe}:x_{Ni}$ to vary, which it does according to experiment (from 0.127 in the matrix to up to 0.16 at the grain boundary). The only other change is an extension of the assumption that the C activity is uniform. The new assumption is that the activities of B and C are uniform.

The first step in calculating the matrix composition at the grain boundary is to calculate the activities of all species in the bulk using equations (2) and (3). This calculation requires only the specification of temperature and the bulk composition. This yields the quantities $a_B$, $a_C$, and $a_{Fe}/a_{Ni}$ for the steps that will follow.

It is important to recognize this procedure is strictly valid at time = 0. For later times, the bulk carbon activity will decrease substantially due to the precipitation of chromium carbides. Simulations of the loss of carbon from the matrix to the precipitates have been made using the program DEPLETE [1], and show that the carbon loss is negligible for the cases of interest. For example, $x_{Cr,gb}$, which depends on $a_C$, increases by 0.2 at.% between 0 and 250 h at 873 K and by 0.5 at.% between 0 and 10 h at 973 K.

The second step in calculating the matrix composition at the grain boundary is to calculate the activity of chromium at the grain boundary, $a_{Cr,gb}$. By the assumption of local chemical equilibrium between the chromium carbide and the matrix, $a_{Cr,gb}$ can be obtained by writing a relation describing the chemical equilibrium between Cr, C, and the chromium carbide. For $Cr_7C_3$, the equation is

$$a_{Cr,gb}^7 a_C^3 = \exp(\Delta G^0_{Cr_7C_3}/RT)$$

or, solving for $a_{Cr,gb}$,

$$a_{Cr,gb} = a_C^{-3/7} \exp(\Delta G^0_{Cr_7C_3}/7RT) \qquad (4)$$

Table 6. Calculated grain boundary compositions for an alloy containing Ni–16 Cr–9 Fe–0.026 C

| Precipitate | Cr concentration (at%) | | Fe concentration/Ni concentration | |
|---|---|---|---|---|
| $T$(K) | $Cr_7C_3$ | $Cr_{23}C_6$ | $Cr_7C_3$ | $Cr_{23}C_6$ |
| 873 | 6.5 | 12.0 | 0.169 | 0.146 |
| 973 | 9.1 | 15.0 | 0.154 | 0.133 |
| 1073 | 12.1 | 18.0 | 0.139 | 0.123 |

where $a_C$ is the bulk activity of carbon that was calculated previously and the free energy of formation is in $J$/g-mol. A similar equation can be written for $Cr_{23}C_6$. The Cr content at the grain boundary cannot be calculated directly from equation (4), because the activity coefficient is a non-linear function of the as-yet unknown concentrations.

Now that the quantities $a_B$, $a_C$, $a_{Cr,gb}$, and $a_{Fe}/a_{Ni}$ are available, the composition at the grain boundary can be calculated. Since there are five unknown components of composition (B, C, Cr, Fe, Ni) at the grain boundary, five equations are required. These are

$$0 = a_B(\mathbf{X}) - a_B \tag{5a}$$

$$0 = a_C(\mathbf{X}) - a_C \tag{5b}$$

$$0 = a_{Cr,gb}(\mathbf{X}) - a_{Cr,gb} \tag{5c}$$

$$0 = a_{Fe}(\mathbf{X})/a_{Ni}(\mathbf{X}) - a_{Fe}/a_{Ni} \tag{5d}$$

$$0 = 1 - \sum_i x_i \tag{5e}$$

where $a_B$, $c_C$, and $a_{Fe}/a_{Ni}$ are the values calculated for the bulk composition, $a_{Cr,gb}$ is the value obtained from equation (4), $\mathbf{X}$ is a short-hand notation for the 5 components of the composition (the unknowns), and $a_i(\mathbf{X})$ is the activity of component $i$ at the grain boundary calculated using equations (2) and (3) with the composition at the grain boundary. The set of composition components $\mathbf{X}$ that satisfies equation 5(a)–(e) is the composition of the matrix at the grain boundary.

Equation 5(a)–(e) are non-linear, and must be solved iteratively. This was done using the Newton–Raphson method [32].

The results of a simulation of the matrix composition at the grain boundary of the C-doped alloy are shown in Table 6. The table contains the model results for $x_{Cr,gb}$ and the ratio of the iron to the nickel grain boundary concentration ($x_{Fe}/x_{Ni}$) for grain boundaries covered by both $Cr_7C_3$ and $Cr_{23}C_6$. The results for both precipitates are presented to indicate the theoretical increase in the grain boundary Cr concentration expected with the precipitation of $Cr_{23}C_6$. As the table shows, precipitation of $Cr_{23}C_6$ would increase the Cr concentration minimum by over 5 at.%.

The validity of the model can be checked by comparing its results with experimental grain boundary composition results. The experimental values for $x_{Cr,gb}$ and $x_{Fe}/x_{Ni}$ shown in Table 3 correspond fairly well to the model results at 873 and 973 K, but not at 1073 K (Table 6). Since the model correctly determines the measurable components at the grain boundaries (Cr, Fe, and Ni) in both alloys at the lower temperatures, it will be used to provide the chemical activities of all five species at the grain boundary as required by equation 13(a)–(c) below.

The chromium depletion minima were recalculated to account for the presence of B in the matrix. Assuming no effect of B on precipitate composition, there was no effort of B on the calculated grain boundary concentrations. This is understandable, because, given the parameters used in equation (3), small quantities of B should not have any significant effect on the activities of the other components present in the matrix.

### *4.3. Precipitate composition*

A thermodynamic model has been constructed to describe the partitioning of elements into $M_7X_3$ and $M_{23}X_6$. This model will be used to explain the experimental observations regarding precipitate type and composition. For convenience, these precipitates will both be represented as $M_mN_n$, with $m + n = 1$. For the cases of interest, $M$ can be any one of three metals (Cr, Fe, or Ni), and $N$ can be either of two non-metals (B or C).

The calculation of precipitate composition begins with the consideration of the free energy of formation that accompanies the creation of 1 g-atom of precipitate from the matrix. The minimization of this free energy change will ultimately yield the composition of the precipitate. The formation of the general five component precipitate is represented by the chemical reaction

$$m_1\,\mathrm{Cr} + m_2\,\mathrm{Fe} + m_3\,\mathrm{Ni} + n_1\,\mathrm{B} + n_2\,\mathrm{C} \leftrightarrow (\mathrm{Cr}_{m_1/m}\mathrm{Fe}_{m_2/m}\mathrm{Ni}_{m_3/m})_m(\mathrm{B}_{n_1/n}\mathrm{C}_{n_2/n})_n \tag{6}$$

where $m_i$ represents the number of moles of the metal $M_i$, and $n_j$ represents the number of moles of the non-metal $N_j$. From equation (6), the free energy change associated with the creation of one gram-mole of precipitate can be written as

$$\Delta G^0_{ppt} = G^0_{ppt} - \sum_i m_i\mu_i - \sum_j n_j\mu_j \tag{7}$$

where $G^0_{ppt}$ is the free energy of formation of the mixed precipitate and $\mu_i$ and $\mu_j$ are the chemical potentials of all species in the matrix. Using equation (2), the free energy change can be re-written

$$\Delta G^0_{ppt} = G^0_{ppt} - RT\sum_i m_i \ln a_i - RT\sum_j n_j \ln a_j. \tag{8}$$

Minimization of equation (8) will yield the precipitate composition.

A model must be chosen to estimate $G^0_{ppt}$, because $G^0_{ppt}$ is not available for the mixed $M_{23}X_6$ and $M_7X_3$ precipitates. The model chosen is the simplest one available. Here, $G^0_{ppt}$ is represented by

$$G^0_{ppt} = \sum_i \sum_j (m_i/m)(n_j/n)G^0_{ij} + RT \sum_i m_i \ln m_i/m + RT \sum_j n_j \ln n_j/n. \quad (9)$$

where $G^0_{ij}$ is the free energy of formation of the precipitate $(M_i)_m(N_j)_n$. The first term is a weighted sum of the free energies of formation of all the constituent binary compounds. The remaining terms represent the ideal entropies of mixing on the respective metallic and non-metallic atom sublattices. This is to say that each sublattice is considered to be an ideal solution. This model implicitly assumes that there are no defects in these precipitates, and that strain and surface energy contributions are insignificant. This representation of $G^0_{ppt}$ has been used previously for mixed, stoichiometric compounds [33, 34]. Equation (9) can be inserted into equation (8). Substituting the variables $M_i \equiv m_i/m$ and $N_j \equiv n_j/n$ then yields

$$\Delta G^0_{ppt} = \sum_i \sum_j M_i N_j G^0_{ij} + mRT \times \sum_i M_i \ln M_i/a_i + nRT \sum_j N_j \ln N_j/a_j. \quad (10)$$

Because of the definitions of $M_i$ and $N_j$, we have

$$\sum_i M_i = 1, \quad (11a)$$

and

$$\sum_j N_j = 1. \quad (11b)$$

Equation (10) is the particular form of equation (8) that will be used to minimize $\Delta G^0_{ppt}$. It represents $\Delta G^0_{ppt}$ as a function of five unknowns ($M_i$, $N_i$). One method for minimizing such an equation is through the use of LaGrange multipliers. This yields the following relations

$$\frac{\partial \Delta G^0_{ppt}}{\partial M_1} = \frac{\partial \Delta G^0_{ppt}}{\partial M_2} \quad (12a)$$

$$\frac{\partial \Delta G^0_{ppt}}{\partial M_1} = \frac{\partial \Delta G^0_{ppt}}{\partial M_3} \quad (12b)$$

$$\frac{\partial \Delta G^0_{ppt}}{\partial N_1} = \frac{\partial \Delta G^0_{ppt}}{\partial N_2}. \quad (12c)$$

Calculating these derivatives using equation (10) and rearranging yields equation 13(a)–(c):

$$0 = \sum_j N_j(G^0_{2j} - G^0_{1j}) + mRT \ln(M_2 a_{M_1}/M_1 a_{M_2}) \quad (13a)$$

$$0 = \sum_j N_j(G^0_{3j} - G^0_{1j}) + mRT \ln(M_3 a_{M_1}/M_1 a_{M_3}) \quad (13b)$$

$$0 = \sum_i M_j(G^0_{i2} - G^0_{i1}) + nRT \ln(N_2 a_{N_1}/N_1 a_{N_2}). \quad (13c)$$

Together, equations 11(a)–(b) and 13(a)–(c) yield five equations in five unknowns. Because these are non-linear, they are solved using the Newton–Raphson method. Two precautions are required. An initial search of the composition field is made to prevent the solution from approaching the maximum in $\Delta G^0_{ppt}$ instead of the minimum. In addition, changes in the composition vectors are restricted to maintain the constraints $0 < M_i, N_j < 1$.

The only parameters required are the activities of the five components ($a_i$, $a_j$) in the face centered cubic matrix and the 12 free energies of formation, $G^0_{ij}$ (six for each type of precipitate). The matrix activities are chosen in two ways. If the temperature is at or above the $Cr_7C_3$ solvus, the activities are the bulk activities. If the temperature is below the $Cr_7C_3$ solvus, the activities are calculated for a matrix in local equilibrium with $Cr_7C_3$ using the grain boundary composition model. This is done because the experiments discussed above showed $Cr_7C_3$ to be the dominant grain boundary precipitate for the alloys of interest, and that it controls the grain boundary composition.

The model could be extended by iterating on the grain boundary composition and then recalculating the precipitate composition. The grain boundary composition is calculated for equilibrium with a grain boundary containing pure $Cr_7C_3$, and not for $M_7X_3$ containing Fe, Ni, and B as well. The grain boundary composition could be recalculated given the solution of the $M_7X_3$ composition. This would yield new activities in equilibrium with the $M_7X_3$ precipitate. The $M_7X_3$ composition itself could then be corrected. However, these iterations are not necessary for $M_7X_3$, because it is always highly rich in Cr and C.

The choice of grain boundary activities calculated for $Cr_7C_3$ might seem inappropriate for use in the calculation of the $M_{23}X_6$ composition. However, the experimental Cr depletion results are similar with and without B, and Cr + C-rich $M_7X_3$ is always the dominant precipitate. Therefore, $M_{23}X_6$ precipitates grow in an environment described by the $Cr_7C_3$ depletion model, and the same local matrix composition can be used as for the $M_7X_3$ calculation.

The $G^0_{ij}$ required by the precipitate composition model were chosen from the literature when reliable data were available, and were estimated in other cases. Reliable data appear in the literature for $Cr_7C_3$, $Fe_7C_3$, $Cr_{23}C_6$, and $Fe_{23}C_6$. The $G^0_{ij}$ of the remaining compounds were estimated. This was done by applying the precipitate composition model to ternary compounds and using ternary phase diagram

Table 7. Differences in the free energies of formation of $M_7X_3$ and $M_{23}X_6$ with their isomorphous chromium carbides (J/g-mol)

| M–X | $G^0(M_7X_3) - G^0(Cr_7C_3)$ | $G^0(M_{23}X_6) - G^0(Cr_{23}C_6)$ | Reference |
|---|---|---|---|
| Cr–B | 32,866 | 125,051 | 35 |
| Fe–B | 8,766 | 82,902 | 36 |
| Ni–B | −7564 | −32,294 | 37, 28 |
| Fe–C | 200,000 | 400,000 | 38, 39 |
| Ni–C | 332,295 | 608,901 | 40 |

information available in the literature to evaluate the unknown $G^0_{ij}$ [23]. The differences in free energies of formation [see equation 13(a)–(c)] for the various isomorphous compounds are summarized in Table 7. These differences were calculated by evaluating the free energies of the various compounds at particular temperatures and subtracting the values for the pertinent chromium carbides at those temperatures. Due to a lack of detailed information, the differences in free energy are themselves assumed to be temperature independent. Also included in Table 7 are the differences for the iron carbides. These numbers were chosen by considering data on $G^0(Fe_7C_3)$ and $G^0(Fe_{23}C_6)$ in the literature [38, 39]. The expressions for the free energies of formation of the chromium carbides were derived from Ref. [41]

$$G^0(Cr_7C_3) = -174511.0 - 25.764\,T \text{ J/g-mol} \quad (14)$$

$$G^0(Cr_{23}C_6) = -411204.0 - 38.66\,T \text{ J/g-mol}. \quad (15)$$

The results for the behaviour of $M_7X_3$ are similar for both the C-doped and the B + C-doped alloys (Table 8). According to the model, the precipitates should be stable below about 1243 K in both cases. Moreover, they should be rich in Cr and C. No essential differences in the $M_7X_3$ compositions due to the presence of B are found. In particular, the model fails to explain the occurrence of a B-rich form of $M_7X_3$ at 1373 K.

The model predicts significantly different compositions of $M_{23}X_6$ in the two alloys (Table 9). In particular, the C-doped alloy should contain Cr + C-rich $M_{23}X_6$ with significant Fe and Ni below 1073 K, but the B + C-doped alloy should contain Ni + B-rich $M_{23}X_6$. At 1373 K, the $M_{23}X_6$ is found to be unstable with respect to the matrix, in that $\Delta G$ is positive, and the most stable composition is predicted to be Cr + C-rich. Thus, the model fails to agree with experimental observations at this temperature.

Table 9. Model results for composition of intergranular $M_{23}X_6$ in Ni–16 Cr–9 Fe (results expressed in $100 \times M_i$ or $100 \times N_j$)

| Alloy | Temperature (K) | $M_{Cr}$ | $M_{Fe}$ | $M_{Ni}$ | $N_B$ | $N_C$ |
|---|---|---|---|---|---|---|
| C-doped | 873 | 62.6 | 13.1 | 24.3 | 0 | 100 |
| | 973 | 62.8 | 14.7 | 22.5 | 0 | 100 |
| | 1373[a] | 51.6 | 26.5 | 21.9 | 0 | 100 |
| B + C-doped | 873 | 2.3 | 7.1 | 90.7 | 99.8 | 0.2 |
| | 973 | 3.8 | 10.0 | 86.2 | 99.3 | 0.7 |
| | 1373[a] | 48.1 | 27.5 | 24.4 | 6.2 | 93.8 |

[a]Precipitate is unstable with respect to matrix.

## 5. DISCUSSION

### 5.1. Precipitate composition

The precipitate composition model was used to calculate the compositions of lowest free energy for both $M_7X_3$ and $M_{23}X_6$. This model is in good qualitative agreement with the experimental results at 873 and 973 K in that the model calculations yield the result of Cr + C-rich $M_7X_3$, with over 90 at.% Cr and approximately 100 at.% C on the respective sublattices at these temperatures. In addition, the model correctly predicts that $M_{23}X_6$ grain boundary precipitates should contain over 80 at.% Ni on the metallic sublattice, and 100 at.% B on the non-metallic sublattice at these temperatures.

Model calculations show that the Ni + B-rich $M_{23}X_6$ phase forms *only* when the chemical activities in the matrix are chosen for a grain boundary in equilibrium with $Cr_7C_3$. Use of the bulk activities in such calculations yields Cr + C-rich precipitates, with $M_{Cr} = 0.934$ at 873 K and 0.916 at 973 K, and $N_C \sim 1$ in both cases ($M_i$ = atom fraction of $i$ in the metallic sublattice, $N_j$ = atom fraction of $j$ in the non-metallic sublattice). Thus, it appears that the composition of $M_{23}X_6$ is determined by the local environment. Specifically, it depends on the low Cr activity and

Table 8. Model results for the composition of intergranular $M_7X_3$ in Ni–16 Cr–9 Fe (results expressed in $100 \times M_i$ or $100 \times N_j$)

| Alloy | Temperature (K) | $M_{Cr}$ | $M_{Fe}$ | $M_{Ni}$ | $N_B$ | $N_C$ |
|---|---|---|---|---|---|---|
| C-doped | 873 | 93.8 | 4.2 | 2.0 | 0 | 100 |
| | 973 | 92.1 | 5.4 | 2.5 | 0 | 100 |
| | 1373[a] | 79.3 | 15.3 | 5.3 | 0 | 100 |
| B + C-doped | 873 | 93.4 | 4.5 | 2.1 | 0 | 100 |
| | 973 | 91.7 | 5.7 | 2.6 | 0.006 | 99.94 |
| | 1373[a] | 78.9 | 15.6 | 5.5 | 0.9 | 99.1 |

[a]Precipitate is unstable with respect to matrix.

high Ni and Fe activities at the grain boundary due to the growth of Cr-rich $M_7C_3$.

This is a particularly significant conclusion. It means that if $Cr_{23}C_6$ were to form, another boride would be expected. In addition, it suggests that Ni + B-rich $M_{23}X_6$ cannot alter Cr depletion, because it is a *consequence* of Cr depletion.

Simple chemical reactions can be written to uncover the sensitivity of the model to the various parameters. According to the thermodynamic model, $M_{23}X_6$ is most stable if it is rich in Ni and B and poor in Cr and C. This result can be understood by inspecting the reaction

$$Cr_{23}C_6 + 23\,Ni + 6\,B \rightarrow Ni_{23}B_6 + 23\,Cr + 6\,C. \quad (16)$$

The free energy change for this reaction is

$$\Delta G(Cr_{23}C_6 \rightarrow Ni_{23}B_6) = G^0(Ni_{23}B_6) - G^0(Cr_{23}C_6) + 23\,\mu_{Cr} - 23\,\mu_{Ni} + 6\,\mu_C - 6\,\mu_B. \quad (17)$$

For the B-doped alloy at 973 K, using values for the chemical potential from the grain boundary, we have $\mu_{Cr} = -20{,}900$, $\mu_{Ni} = -2260$, $\mu_C = -17{,}800$, and $\mu_B = -74{,}600$ J/g-mol. Taking $G^0(Ni_{23}B_6) - G^0(Cr_{23}C_6) = -32{,}293$ J/g-mol, the free energy change is $\Delta G(Cr_{23}C_6 \rightarrow Ni_{23}B_6) = -120{,}000$ J/g-mol. Since this free energy change is negative, $Ni_{23}B_6$ is relatively stable with respect to $Cr_{23}C_6$. Using bulk values for the chemical potentials, we have $\mu_{Cr} = -12{,}300$ J/g-mol, $\mu_{Ni} = -3550$ J/g-mol, and $\Delta G(Cr_{23}C_6 \rightarrow Ni_{23}B_6) = +107{,}000$ J/g-mol. This again shows that the presence of $Ni_{23}B_6$ instead of $Cr_{23}C_6$ is a consequence of the changes in chemical potentials caused by the growth of $Cr_7C_3$.

A similar analysis can be applied to $M_7X_3$. The reaction to consider is

$$Cr_7C_3 + 7\,Ni + 3\,B \rightarrow Ni_7B_3 + 7\,Cr + 3\,C. \quad (18)$$

The free energy change for this reaction is

$$\Delta G(Cr_7C_3 \rightarrow Ni_7B_3) = G^0(Ni_7B_3) - G^0(Cr_7C_3) + 7\,\mu_{Cr} - 7\,\mu_{Ni} + 3\,\mu_C - 3\,\mu_B. \quad (19)$$

For the B-doped alloy at 973 K, using the same values at the grain boundary as before, and letting $G^0(Ni_7B_3) - G^0(Cr_7C_3) = -7564$, we have $\Delta G(Cr_7C_3 \rightarrow Ni_7B_3) = +32{,}400$ J/g-mol. Since this quantity is positive, $Cr_7C_3$ is relatively stable with respect to $Ni_7B_3$.

The dependence of Ni + B-rich $M_{23}X_6$ on Cr-rich $M_7C_3$ is a conclusion based on calculations using the data sets in the tables. A possible objection to this conclusion is that the results are sensitive to parameter choices. However, the following arguments demonstrate that the model results will only change substantially if major changes are made in the data set. The data set used in the calculations yields good estimates of the grain boundary composition, which means that the computed activities (or chemical potentials) of C, Cr, Fe, and Ni are valid both at and away from the grain boundary. When the grain boundary chemical potentials are used with the best estimate for the quantity $DG^0 \equiv G^0(Ni_{23}B_6) - G^0(Cr_{23}C_6)$, the free energy change for the transformation of $Cr_{23}C_6$ to $Ni_{23}B_6$ is $-120{,}000$ J/g-mol. The corresponding calculation using bulk chemical potentials yields + 107,000 J/g-mol. This large difference cannot be accounted for by modest perturbations of $DG^0$. The only other free parameter is the chemical potential of B. In order to change the sign of the free energy change for transformation, a change in $\mu_B$ on the order of 20,000 J/g-mol is required, which represents a factor of 12 change in the activity of B. Thus, large changes in the best estimates of $a_B$ and $DG^0$ would be required to calculate either Ni + B-rich $M_{23}X_6$ with bulk activities or Cr + C-rich $M_{23}X_6$ with grain boundary activities.

The main deficiency of the model is its failure to explain high temperature precipitation. At 1373 K, the compositions of highest stability are unstable with respect to the matrix by approximately 9860 J/g-mol of $M_{23}X_6$ and 7500 J/g-mol of $M_7X_3$. In addition, the metallic compositions of the model are not in agreement with experiment.

It can again be asked whether the model results are sensitive to the parameters chosen. Since the free energy differences between precipitate and matrix listed above are small, reasonable parameter variations might be expected to yield the prediction of stable precipitates at high temperature. For example, doubling the original values used for B activities results in the prediction of stable $M_{23}X_6$ at all temperatures up through 1673 K. At 1373 K, the calculated composition of $M_{23}X_6$ is $M_{Cr} = 0.107$, $M_{Fe} = 0.254$, $M_{Ni} = 0.639$, $N_B = 0.905$, and $N_C = 0.095$, and this is stable with respect to the matrix by $-15080$ J/g-mol. The metallic sublattice composition is in fair accord with the measurements for $M_{23}X_6$ at 1373 K (Table 2). A doubling of $a_B$ has virtually no effect on either the calculated $M_7X_3$ composition or its stability. In summary, the high temperature precipitation of $M_{23}X_6$ can be explained by doubling $a_B$, but the precipitation of $M_7X_3$ cannot.

The sensitivity of the model results to the data set may also be tested by perturbing the estimated free energies of formation. For example, reducing $G^0(Ni_7C_3)$ by 100,000 J/g-mol yields a calculated composition $M_{Cr} = 0.685$, $M_{Fe} = 0.139$, $M_{Ni} = 0.176$, $N_B = 0.017$, and $N_C = 0.983$, and $DG = -3100$ J/g-mol at 1373 K. However, this is not a modest perturbation. Small, individual perturbations of the original data base do not yield calculations of stable $M_7X_3$ at high temperature.

### 5.2. *Stability of $Cr_{23}C_6$ and $Cr_7C_3$*

The absence of intergranular $Cr_{23}C_6$ in the B free alloy requires some discussion. According to the

precipitate composition model, it is stable below 1073 K (Table 9). However, the corresponding high grain boundary Cr concentrations suggest that the driving force for $Cr_{23}C_6$ is relatively small. This can be demonstrated more clearly by calculating the relative stability of $Cr_{23}C_6$ and $Cr_7C_3$ in Ni–18 at.% Cr–9 at.% Fe using two separate reactions. The first is the addition of Cr to $Cr_7C_3$ after the precipitate has formed. This is represented by

$$2\,Cr_7C_3 + 9\,Cr \rightarrow Cr_{23}C_6. \quad (20)$$

The free energy change for this reaction is

$$\Delta G(2\,Cr_7C_3 \rightarrow Cr_{23}C_6) = G^0(Cr_{23}C_6) - 2\,G^0(Cr_7C_3) - 9\,\mu_{Cr}. \quad (21)$$

The calculated values of the chemical potentials in the bulk at 973 K are $\mu_C = -17{,}800$ and $\mu_{Cr} = -12{,}300$ J/g-mol. Using equations (14) and (15), $G^0(Cr_7C_3) = -199{,}575$ J/g-mol and $G^0(Cr_{23}C_6) = -448{,}820$ J/g-mol. This yields $\Delta G(2\,Cr_7C_3 \rightarrow Cr_{23}C_6) = +61{,}000$ J/g-mol. Since $\Delta G(2\,Cr_7C_3 \rightarrow Cr_{23}C_6)$ is positive, $Cr_7C_3$ is relatively stable with respect to $Cr_{23}C_6$. At the grain boundary, $\mu_{Cr}$ is smaller, and makes the result even more positive, so that chromium depletion enforces the relative stability of $Cr_7C_3$. The second reaction to consider is the decomposition of $Cr_7C_3$. This is represented by

$$3.286\,Cr_7C_3 \rightarrow Cr_{23}C_6 + 3.857\,C. \quad (22)$$

The free energy change for this reaction is

$$\Delta G(3.3\,Cr_7C_3 \rightarrow Cr_{23}C_6) = G^0(Cr_{23}C_6) + 3.857\,\mu_C - 3.286\,G^0(Cr_7C_3). \quad (23)$$

Using the parameters listed above, equation (23) yields $\Delta G(3.3\,Cr_7C_3 \rightarrow Cr_{23}C_6) = +138{,}000$ J/g-mol. Since this quantity is positive, $Cr_7C_3$ is relatively stable. In summary, $Cr_7C_3$ is stable relative to $Cr_{23}C_6$ regardless of path.

The arguments above show that the thermodynamic driving force for $Cr_{23}C_6$ is weaker than that for $Cr_7C_3$. This alone is sufficient to explain the absence of intergranular $Cr_{23}C_6$. Intragranular $Cr_{23}C_6$ does appear in the C-doped alloy following heat treatments of 973 K for 100 h [25], and the isomorphous precipitate $M_{23}X_6$ forms if B is added. Given these experimental facts, $Cr_{23}C_6$ should be able to nucleate and grow on grain boundaries in Ni–16 Cr–9 Fe. Its absence should not be attributed to kinetic limitations, but rather to a stronger driving force for $Cr_7C_3$.

## 6. CONCLUSIONS

1. A thermodynamic model has been constructed to explain the intergranular precipitation behavior of Ni–16 Cr–9 Fe doped with C and B. The model results are consistent with the presence of Cr-rich $M_7C_3$ and Ni + B-rich $M_{23}X_6$ and the absence of intergranular Cr + C-rich $M_{23}X_6$ in high purity Ni–16 Cr–9 Fe–0.03 C–0.005 B.

2. Using the carbon and chromium activities generated by a Kohler equation representation of the matrix, $Cr_7C_3$ is thermodynamically stable with respect to $Cr_{23}C_6$ in these alloys.

3. Based on the model of precipitate composition, intergranular Ni + B-rich $M_{23}X_6$ forms at 600–700°C because this is the thermodynamically stable composition for this precipitate at the grain boundary. It forms as a consequence of the low chemical activity of Cr and high chemical activities of Ni and Fe in local equilibrium with intergranular, Cr-rich $M_7C_3$.

4. 50 wppm boron is above the solubility limit at all temperatures up to 1473 K. Intergranular $M_7X_3$ and $M_{23}X_6$, containing B, form at 1373 and 1473 K. This high temperature precipitation is not explained by the precipitate composition model.

*Acknowledgements*—The authors gratefully acknowledge the Electron Microbeam Analysis Laboratory at The University of Michigan, the Center for Materials Science at the Massachusetts Institute of Technology, and the Materials Science Division at Argonne National Laboratory in Illinois for the generous use of equipment. This work was funded by the Office of Basic Energy Sciences of the U.S. Department of Energy under contract DE-FG02-85ER45184.

## REFERENCES

1. G. S. Was and R. M. Kruger, *Acta metall.* **33,** 841 (1985).
2. R. Bandy and R. L. Sabatini, *Corrosion* **41,** 242 (1985).
3. G. P. Airey and F. W. Pement, *Corrosion* **39,** 46 (1983).
4. R. M. Kruger, S. F. Claeys and G. S. Was, *Corrosion* **41,** 504 (1985).
5. C. L. Briant, C. S. O'Toole and E. L. Hall, *Corrosion* **42,** 15 (1986).
6. G. S. Was and V. B. Rajan, *Metall. Trans. A.* To be published.
7. E. L. Hall and C. L. Briant, *Metall. Trans. A* **16A,** 1225 (1985).
8. Ph. Berge, J. R., Donati, D. Guttmann, D. Laurent and S. Palous, *Mém. scient. Revue Metall.* **71,** 773 (1974).
9. V. Lupinc and C. Castani, *Z. Metallk.* **65,** 63 (1974).
10. M. da Cunha Belo, D. Colin, Ph. Berge and Y. Rouillon, *Mém. scient. Revue Metall.* **77,** 887 (1980).
11. G. P. Airey, *Optimization of Metallurgical Variables to Improve the Stress Corrosion Cracking Resistance of Inconel 600,* EPRI NP-1354 (1980).
12. H. Nagano, K. Yamanaka and T. Kudo, *Sumitomo Search* **31,** 129 (1985).
13. M. J. Donachie, *Superalloys Sourcebook.* Am. Soc. Metals, Metals Park (1984).
14. A. K. Sinha and J. J. Moore, *Metallography* **19,** 87 (1986).
15. N. J. Zaluzec and J. F. Mansfield, *Inst. Phys. Conf. Ser. No. 78,* p. 173, EMAG '85, Newcastle upon Tyne (1985).
16. J. J. Hren, J. I. Goldstein and D. C. Joy (editors) *Introduction to Analytical Microscopy.* Plenum Press, New York (1983).
17. G. S. Was and J. R. Martin, *Metall. Trans. A* **16A,** 349 (1985).
18. D. J. Dyson and K. W. Andrews, *J. Iron Steel Inst.* **207,** 208 (1969).
19. A. L. Bowman, G. P. Arnold, E. K. Storms and N. G. Nereson, *Acta crystallogr.* **B28,** 3102 (1972).

20. H. H. Stadelmaier, in *Developments in the Structural Chemistry of Alloy Phases* (edited by B. C. Giessen). Plenum Press, New York (1969).
21. M. H. Lewis and B. Hattersley, *Acta metall.* **13,** 1159 (1965).
22. J. W. Edington, *Practical Electron Microscopy in Materials Science*. Van Nostrand Reinhold, New York (1976).
23. R. M. Kruger, thesis, Univ. of Michigan (1987).
24. R. M. Kruger and G. S. Was, *Metall. Trans. A*. To be published.
25. F. Kohler, *Monatsh. Chem.* **91,** 738 (1960).
26. L. Kaufman and H. Nesor, in *Treatise on Solid State Chemistry 6* (edited by N. B. Hannay). Plenum Press, New York (1975).
27. L. Kaufman and H. Nesor, *Calphad* **2,** 295 (1978).
28. L. Kaufman, B. Uhrenius, D. Birnie and K. Taylor, *Calphad* **8,** 25 (1984).
29. L. Kaufman, *Calphad* **1,** 7 (1977).
30. K. Lobl, H. Tuma and M. Ciznerova, *Mém. Revue Scient. Metall.* **71,** 271 (1974).
31. T. Wada, H. Wada, J. F. Elliott and J. Chapman, *Metall. Trans.* **2,** 2199 (1971).
32. W. Kaplan, *Advanced Mathematics for Engineers*. Addison-Wesley, Reading, Mass. (1981).
33. M. Hillert, in *Phase Transformations*. Am. Soc. Metals, Metals Park, Ohio (1968).
34. E. Rudy, *J. less-common Metals* **33,** 43 (1973).
35. G. Pradelli, *Metall. Ital.* **66,** 551 (1974).
36. M. Lucco Borlera and G. Pradelli, *Metall. Ital.* **59,** 907 (1967).
37. M. Ayel, R. Riviere and G. Monnier, *Cor. Acad. Sci.* **264,** 1756 (1967).
38. H. Wada, *Metall. Trans.* **16A,** 1479 (1985).
39. M. Waldenstrom and B. Uhrenius, *Scand. J. Metall.* **6,** 202 (1977).
40. W. Koster and S. Kabermann, *Archs Eisenhutt.* **26,** 627 (1955).
41. O. Kubachewskii, E. L. L. Evans and C. B. Alcock, *Metallurgical Thermochemistry*, 4th edn. Pergamon Press, Oxford (1967).